Fall 2022

An Initial Study of Properties of Monolithic Silicon Dioxide Parts Produced by the Ceramic on-Demand Extrusion Process

Sam Sujit Choppala
San Jose State University

Recommended Citation

Choppala, Sam Sujit, "An Initial Study of Properties of Monolithic Silicon Dioxide Parts Produced by the Ceramic on-Demand Extrusion Process" (2022). *Master's Theses*. 5330.
DOI: https://doi.org/10.31979/etd.6d5u-u9hy
https://scholarworks.sjsu.edu/etd_theses/5330

AN INITIAL STUDY OF PROPERTIES OF MONOLITHIC SILICON DIOXIDE PARTS PRODUCED BY THE CERAMIC ON-DEMAND EXTRUSION PROCESS

A Thesis

Presented to

The Faculty of the Department of Mechanical Engineering

San José State University

In Partial Fulfillment

of the Requirements for the Degree

Master of Science

by

Sam Sujit Choppala

December 2022

The Designated Thesis Committee Approves the Thesis Titled

AN INITIAL STUDY OF PROPERTIES OF MONOLITHIC SILICON DIOXIDE PARTS PRODUCED BY THE CERAMIC ON-DEMAND EXTRUSION PROCESS

by

Sam Sujit Choppala

APPROVED FOR THE DEPARTMENT OF MECHANICAL ENGINEERING

SAN JOSÉ STATE UNIVERSITY

December 2022

Amir Armani, Ph.D.	Department of Mechanical Engineering
Vimal Viswanathan, Ph.D.	Department of Mechanical Engineering
Raymond Yee, Ph.D.	Department of Mechanical Engineering

ABSTRACT

AN INITIAL STUDY OF PROPERTIES OF MONOLITHIC SILICON DIOXIDE PARTS PRODUCED BY THE CERAMIC ON-DEMAND EXTRUSION PROCESS

by Sam Sujit Choppala

The ceramic on-demand extrusion (CODE) process is an additive manufacturing process for technical ceramics, which features an oil bath and partial drying to print stronger green bodies due to better preservation of the printed specimen structure and reduction of uneven part evaporation. A 3D printer capable of performing the CODE process is built with subsystems including motion, extrusion, and heating, and is controlled through LinuxCNC. The CODE printer and process is tested with silicon dioxide as the technical ceramic. High strength silicon dioxide parts are essential in various present-day industries such as dental, medical, and semiconductor. A 55vol% solids loading slurry feedstock is fed into the extruder and is printed in the shape of ASTM A-sized bars using specific printing parameters. The printed green bodies are subject to post-processing including drying in a humidity chamber and debinding and sintering in a sintering furnace. The density was measured at various sintering schedules for the sintered test specimens. Flexural strength values were obtained by performing a 3-point bending test according to the ASTM C1161 standard, and the mean strength values are reported. Both the density and flexural strength values are lower with printing using CODE when compared to other current additive and conventional manufacturing methods by approximately 32% and 77%, respectively. However, this can be attributed due to defects within the printed parts including porosity due to air pockets and insufficient viscosity when pre-processing the slurry and can be minimized to produce better results.

ACKNOWLEDGEMENTS

First and foremost, I would like to thank my family for providing me with their unconditional love and support throughout all of my academic endeavors. I would like to thank my committee chair, Dr. Amir Armani, for his mentorship, guidance, and financial contribution throughout the duration of this thesis. I would also like to thank my committee members, Dr. Vimal Viswanathan, and Dr. Raymond Yee, for their continued support and feedback. Last, but not least, I would like to thank Armin Allam, Zichen Fang, West Liang, and Dylan Doan for their contribution in assembling the CODE printer.

TABLE OF CONTENTS

LIST OF TABLES

LIST OF FIGURES

LIST OF ABBREVIATIONS

AM – Additive Manufacturing
CODE – Ceramic On-Demand Extrusion
3D – 3-Dimensional
SLA – Stereolithography
DLP – Digital Light Processing
IJP – Inkjet Printing
DIW – Direct Ink Writing
3YSZ – 3mol% Yttria-Stabilized Zirconia
SEVNB – Single Edge V-Notched Beam
CNB – Chevron Notched Beam
3DP – 3D Printing
PLA – Polylactic Acid
GUI – Graphical User Interface
PCIe – Peripheral Component Interconnect Express
MCCB – Molded Case Circuit Breaker
HDPE – High-Density Polyethylene
PVA – Polyvinyl Alcohol
SLS – Selective Laser Sintering

1 INTRODUCTION

1.1 Background

Additive manufacturing (AM) is one of many significant types of manufacturing processes in mechanical engineering. Within the branch of AM, there are several sub-categories that are used to categorize AM processes based on the type of material being used, including metals, ceramics, and plastics. Within additive manufacturing of ceramics, there are further divisions based on the form of feedstock used, including slurry-based, powder-based, and bulk solid-based [1]. Ceramic On-Demand Extrusion (CODE) is a slurry-based 3D printing approach used to print ceramic components. Slurry-based ceramic 3D printing methods use a viscous paste which contain ceramic particles as feedstock. The viscosity and composition of the paste depends on the method of printing. Other slurry-based methods include stereolithography (SLA), digital light processing (DLP), inkjet printing (IJP), direct ink writing (DIW), etc.

The process of CODE involves a slurry feedstock, which is composed of water, a binder, a dispersant, and ceramic particles, being extruded onto a build plate. The extruder moves in both the x and y- directions to control the print. The z-axis is independent of the other two axes and controls the height of the build plate. An oil bath is used to submerge each printed layer. The build plate, attached to the z-axis actuator, initially starts above the oil bath. After each layer is printed onto the build plate, a heating lamp is used to partially and uniformly dry the sequentially printed layers. After this process, the build plate lowers such that the initially printed layer is submerged into the oil bath. This process is performed to prevent non-uniform and uneven rate of evaporation while printing the ceramic component. This printing, drying, and submerging process is repeated for each of the sequentially printed layers until the geometry of the ceramic component is completely printed.

After the printing of the green body, post-processing is required to extract the final ceramic component. Within the post-processing phase, there are three stages: bulk drying, debinding, and sintering. The bulk drying is used to remove all water content from the green body. After bulk drying, the ceramic part is then subject to sintering to burn out the binder and other remaining and unwanted particles. Finally, the ceramic component is then subject to sintering at high temperatures to fully densify the part. After this stage, the remaining component is the final ceramic part.

1.2 Research Hypothesis

The hypothesis of this investigation is that the flexural strengths of dense, monolithic ceramic silicon dioxide parts produced by ceramic on-demand extrusion (CODE) exceed flexural strengths of silicon dioxide parts produced by current additive manufacturing (AM) methods used for ceramics.

The rationale behind this hypothesis is that by using an oil bath to prevent non-uniform evaporation while printing, the component is formed without any cracks or warpages due to uneven drying, and by using heat lamp radiation to partially and uniformly dry the sequentially printed layers, the structure of the part is better preserved for post-processing, including final bulk drying, binder removal, and sintering. Due to this process, the final CODE printed ceramic component will have a greater flexural strength compared to specimens fabricated using currently available additive manufacturing methods for ceramics.

1.3 Broader Impact

The usage of high-strength silicon dioxide (i.e., silica) components is essential in diverse industries. Silicon dioxide is a versatile ceramic used in various applications, and in certain applications high-strength components are required. Specific examples of the uses of silica include shells and cores in aerospace and energy industries, dental industries, and IC applications [2],[3],[4]. Synthetic fused silica is highly used in semiconductor applications, specifically as the optical material for microlithography due to its high deep ultraviolet transmissivity and low absorption [5]. Furthermore, it is highly durable to ultraviolet radiation. Due to its high melting point, silicon dioxide is also used in the construction industry, specifically in the form of silica sand [6]. With regards to medical applications, silicon dioxide is also used as a binding layer for bone prosthetics due to its biocompatibility [7]. Additionally, silica is also used within hybrid materials in the dental industry for implants [8]. Due to the broad and numerous applications of silica, the manufacturing methods of silica components is crucial in producing parts with desired qualities including high strength.

The CODE process is an approach to print parts with greater flexural strengths compared to parts created using other manufacturing methods. Additionally, since the CODE process is currently only tested for two oxides (i.e., alumina and zirconia), further analysis for the CODE process will be achieved using silicon dioxide as the main technical ceramic material. This analysis will support the CODE process by providing additional study to generalize printing with ceramic oxides.

2 LITERATURE REVIEW

2.1 Ceramic On-Demand Extrusion (CODE) Process for Additively Manufactured Ceramics

Current research is being performed to refine the printing of dense parts using the CODE process. Ghazanfari et al. compared mechanical properties such as density, flexural strength, Weibull modulus, Young's modulus, fracture toughness, and hardness of aluminum oxide parts created using CODE with alumina parts produced by other additive manufacturing (AM) processes [9]. This article concluded that many present types of AM processes of ceramics do not produce dense, monolithic ceramic parts with relatively good mechanical properties due to defects such as porosity. The CODE process overcomes this shortcoming by using oil to prevent premature evaporation and heat lamp radiation to create stronger bonds between subsequently printed layers. The CODE method involves controlling several process parameters needed to fabricate a part with favorable properties. Ghazanfari et al. showed by optimizing tool-path planning, drying behavior, extrusion parameters, and binder burnout and sintering schedules that the quality of the fabricated part with regards to the previously mentioned mechanical properties is improved [10]. Ghazanfari et al. used the CODE process to evaluate properties of fully stabilized zirconia parts (8 mol% yttria-stabilized zirconia) and compared the mechanical characteristics to fully stabilized zirconia parts produced by traditional fabrication methods, including cold isostatic pressing [11]. The authors discovered two sintering schedules for the CODE process capable of fabricating fully stabilized zirconia parts with high Vickers hardness and indentation fracture toughness.

Similarly, Li et al. validated the CODE results by examining the mechanical properties of 3 mol% yttria-stabilized zirconia (3YSZ) parts fabricated by CODE and comparing said properties to those of components produced by other ceramic fabrication processes, such as cold uniaxial pressing, selective laser sintering, thermoplastic 3D printing, direct inkjet printing, 3D gel-printing, and lithography-based ceramic manufacturing [12]. Sintering schedules were also examined in this paper, as similar to Ghazanfari et al. [11]; however, for 3YSZ parts, a different sintering schedule was used based on a higher fracture toughness value. Yu et al. also used CODE for fabricating 3YSZ parts [13], which was also performed by Li et al. in [12]; however, the raw powder used was slightly different. The method of testing the mechanical properties as well as the type of mechanical properties tested also differed. For example, Yu et al. used a single edge v-notched beam (SEVNB) method, whereas Li et al. used the chevron notched beam (CNB) method and a compression-compression fatiguing procedure to examine the fracture toughness. Furthermore, different standards were used to study flexural strength, although both papers used the same ASTM C1327 standard to examine hardness [14].

2.2 Testing Methods for Flexural Strength

There are various methods for testing flexural strength as observed in literature. Lu et. al. used a stereolithographic AM process with 3YSZ; however, the tests conducted to measure the mechanical properties of ceramic parts would be universal, regardless of the procedure used in fabrication [15]. This study used both uniaxial and biaxial flexural strength tests, whereas Ghazanfari et al. [11] used only a four-point bending test. The deviation in tests to measure the flexural strength in ceramics could cause a variation in strength values of ceramic parts when comparing flexural strengths of parts produced by CODE to parts manufactured by other fabrication techniques.

2.3 Materials and Forms of Materials Used for Additive Manufacturing of Ceramics

Various ceramic materials can be used in the CODE process to fabricate components in order to observe the deviation of their mechanical properties to the conventional fabrication techniques currently available. For example, Briscoe and Özkan demonstrated that by using alumina with different solvent and plasticizer contents, various ceramic pastes were created, and different hardness values were achieved using the compliance hardness indentation test [16]. These ceramic compositions could be used as material to create parts using CODE as test specimens to compare the performance of this AM method to other manufacturing methods while varying the ratio of materials within the feedstock slurry. Another group of materials used to produce parts by CODE that could be tested for mechanical properties is functionally graded ceramics. Li et al. used CODE to create components graded from pure alumina to an alumina and zirconia mixture with fixed gradients [17]. From the produced parts, the article concluded that high material composition gradients led to increased deformations. Future research could be designed to study the performance of CODE to various functionally graded materials with different gradients.

Further study of mechanical properties such as fracture toughness could be studied to explore the reliability of CODE to produce mechanically favorable, monolithic ceramic parts. Additionally, intricate parts with support structures fabricated by CODE could also be tested to ensure the reliability of the CODE process regardless of the geometric complexity. Li et al. modeled a dual-extruder printing system that contains two separate nozzles to extrude two different materials [18]. This article concluded that printing using calcium carbonate as the support material requires no additional devices for post-processing of the support material.

Their proposed process manages the support structure and properly densifies the final ceramic part.

2.4 Mechanical Properties of Silicon Dioxide Parts Produced by Manufacturing Methods from Current Studies

In order to evaluate the achieved flexural strength of CODE printed silica parts, the flexural strengths of silica components manufactured from other fabrication techniques must be studied. Wang et al. [19] studied silica ceramics created using stereolithography. Wang et al. [16] examined silica ceramics created using digital light processing. Cooperstein et al. used 3D printing (3DP) to create and analyze fused silica ceramics [20]. Wang et al. fabricated and studied the flexural strengths of silica ceramic cores created using DLP [21]. To further compare the flexural strengths of CODE printed parts, studies using conventional manufacturing techniques will also be studied in addition to AM methods. Within conventional approaches, there are two main subcategories: pressure-less sintering and high-pressure sintering. A fair comparison for CODE printed parts would be the pressure-less sintering techniques, as the CODE printed specimens are sintered at atmospheric pressure. Yin et al. used gelcasting to prepare fused silica ceramics subject to sintering without high pressure [22]. Xu et al. created silica ceramics using direct foaming [23]. These mechanical properties studied above from literature are tabulated in Table 1.

Table 1
Mechanical Properties of Silica Parts from Different Manufacturing Methods.

No.	Manufacturing Method	Density [g/cm^3]	Hardness [kg/mm^2]	Flexural Strength [MPa]
1	SLA [19]	1.57	N/A	13.31
2	DLP [24]	1.42	N/A	13.31
3	3DP [20]	1.96	262	N/A
4	DLP [21]	N/A	N/A	13.8
5	Gelcasting [22]	1.78 - 2.05	N/A	20.69
6	Direct Foaming [23]	2.23	N/A	16.3

3 METHODOLOGY

3.1 Building the CODE Printer

The initial phase of testing CODE printed parts involves printing using a 3D printer capable of performing CODE. The physical printer built is a variation of the model created by Ghazanfari et al., which includes several subsystems [10]. The four main subsystems to be controlled include the motion (i.e., gantry) subsystem, extrusion subsystem, heating subsystem, and the electrical subsystem. The assembled physical printer is displayed in Figure 1, which reveals the motion subsystem and the build plate assembled onto the printer frame.

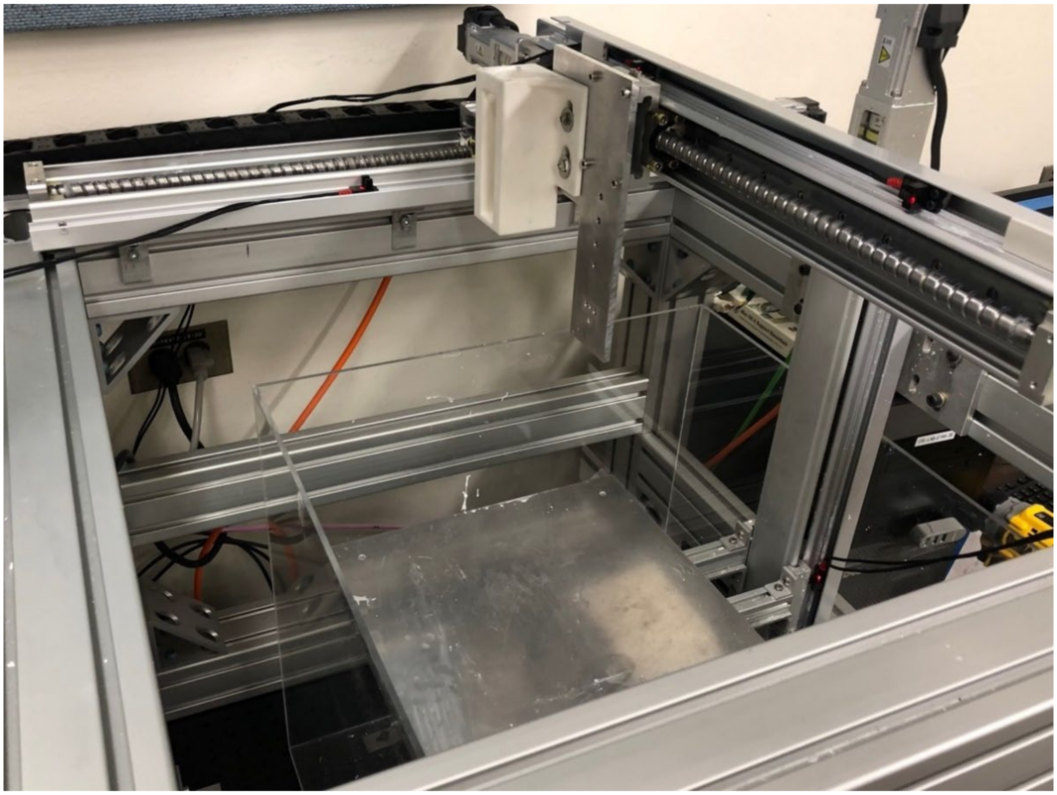

Fig. 1. Assembled physical printer displaying motion subsystem and the build plate.

The motion subsystem consists of three linear actuators controlled by servo motors and drivers to control printing motion spatially in the x-axis, the y-axis, and the z-axis, respectively. The servo motors controlling the linear actuators are 100W Panasonic motors. The linear rails are limited by optical limit switches to control the minimum and maximum positions for each respective axis. All three axes include both motor and encoder connections which drive the corresponding axis as well as report the current position of the axis. Furthermore, the z-axis (i.e., vertical axis) has an independent inbuilt active braking system such that the axis can stop at various levels in the vertical direction, which assists in holding the printing bed. To control the z-axis specifically, the braking system must be powered-on such that the rail is free to move.

The extrusion subsystem is mounted on the y-axis linear actuator of the motion subsystem. The extrusion subsystem consists of an extruder, a mounting bracket, a syringe, tubing, and a feedstock holding bracket, displayed in Figure 2 The mounting bracket connects this subsystem directly onto the y-axis rail, while the extruder and the feedstock holding bracket connects to the mounting bracket. The syringe is placed into the feedstock holding bracket, and the ending of the syringe is connected to the extruder through tubing and an elbow push-connect adapter. The top of the feedstock holding bracket is fitted with a push-connect adapter to allow for inlet compressed air into the syringe and a rubber material for creating a seal such that the compressed air doesn’t leak. The main purpose of the compressed air within the syringe is to force the viscous feedstock into the extruder through the tubing. The mounting bracket is fabricated from 0.25in aluminum and machined to created proper holes according to GD&T standards to minimize vibrations experienced by the extruder due to the movement of the gantry subsystem. The feedstock holding bracket is created by 3D printing with nylon. The main design considerations for this includes supporting the weight of the syringe when filled with feedstock as well as supporting the expansion of the syringe due to pressure from the compressed air.

Fig. 2. Physical extrusion subsystem assembly not including the top cover of the feedstock holding bracket introducing compressed air.

The heating subsystem consists of a heat lamp, a heat lamp mounting frame, a mounting adapter, and aluminum extrusions, displayed in Figure 3. Initially, the heat lamp is connected to the heat lamp mounting frame, and the heat lamp mounting frame is connected to the aluminum extrusions with a mounting adapter. The extrusions were chosen to be fabricated from aluminum to support the weight of the heat lamp and the heat lamp mounting frame, and the mounting adapter was 3D printed using polylactic acid (PLA). The heat lamp is powered by 120VAC and has a power rating of 375W, which is used to partially and uniformly dry each sequentially printed layer. The heat lamp is used to empirically determine the drying time.

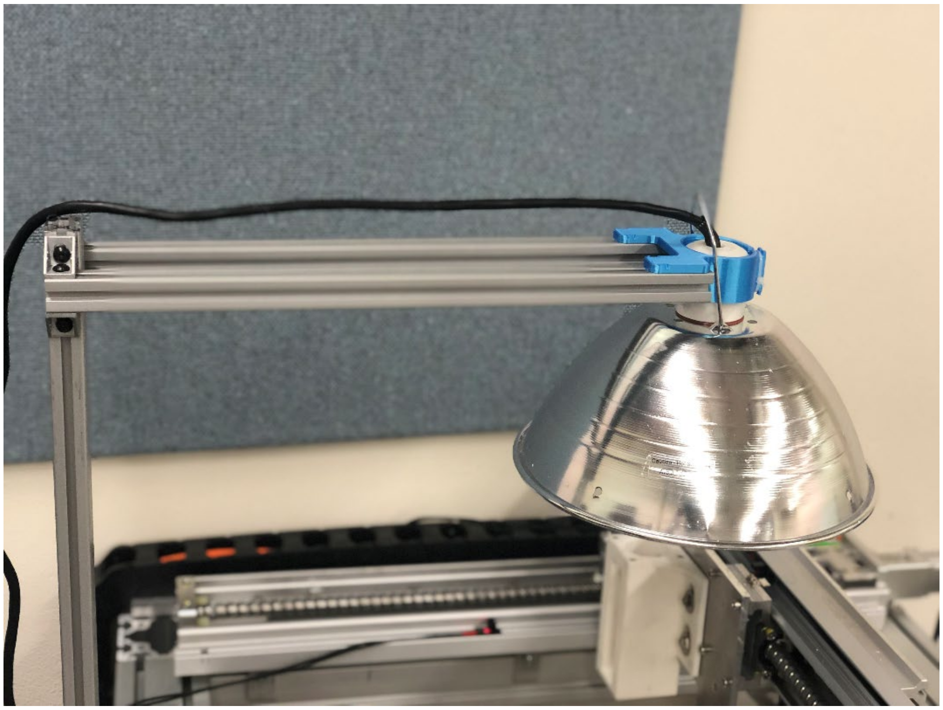

Fig. 3. Physical heating subsystem assembly.

This overall design couples the extruder motion along the x-axis and the y-axis, while the z-axis, which controls the build plate, is independent from the rest of the motion subsystem.

The build plate is composed of two separate plates fabricated from aluminum connected onto the vertical axis with aluminum extrusions as shown in Figure 4. The bottom plate of the print bed directly connects to the extrusions which connect to the vertical axis; however, the top plate connects to the bottom plate with four screws with springs. This design is implemented such that the leveling of the print bed can be individually and freely controlled through the four screws with springs, regardless of the flatness of the bottom plate or the aluminum extrusions that connect to the vertical axis. Additionally, the printer is placed on a four-legged table. This table has pressurized air features such that a continuous inlet of pressurized air is constantly fed into each individual leg of the table. This mechanism creates a damping effect such that the effects of external vibrations are minimized on the printing ability and accuracy of the system. The constant compressed air input is activated throughout the entire printing duration.

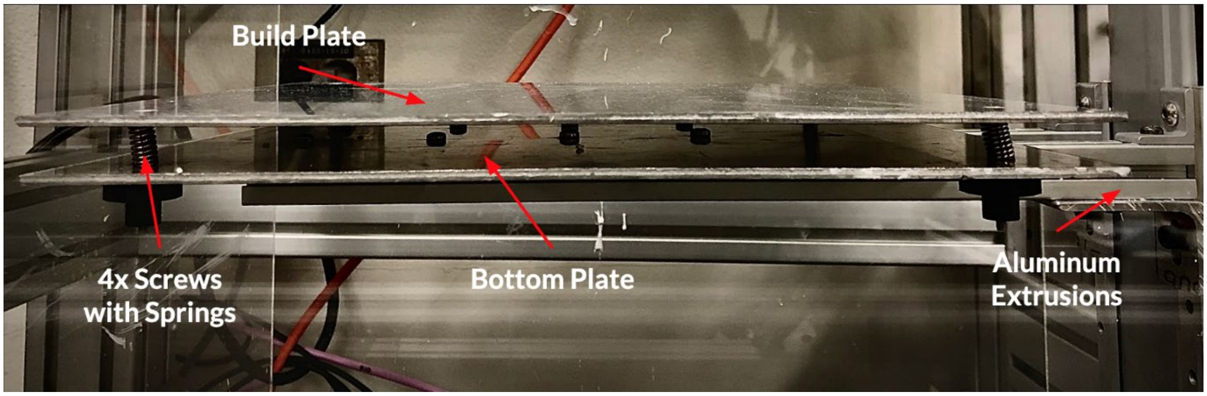

Fig. 4. Build plate mounting assembly.

The electrical subsystem consists of a host computer, power supplies, transformers, circuit breakers, servo motor drivers, programmable boards, a micro-step driver, an electrical relay, breadboards, and intermediate wiring. The overall flowchart displaying the overview of the fully connected electrical subsystem is displayed in Figure 5.

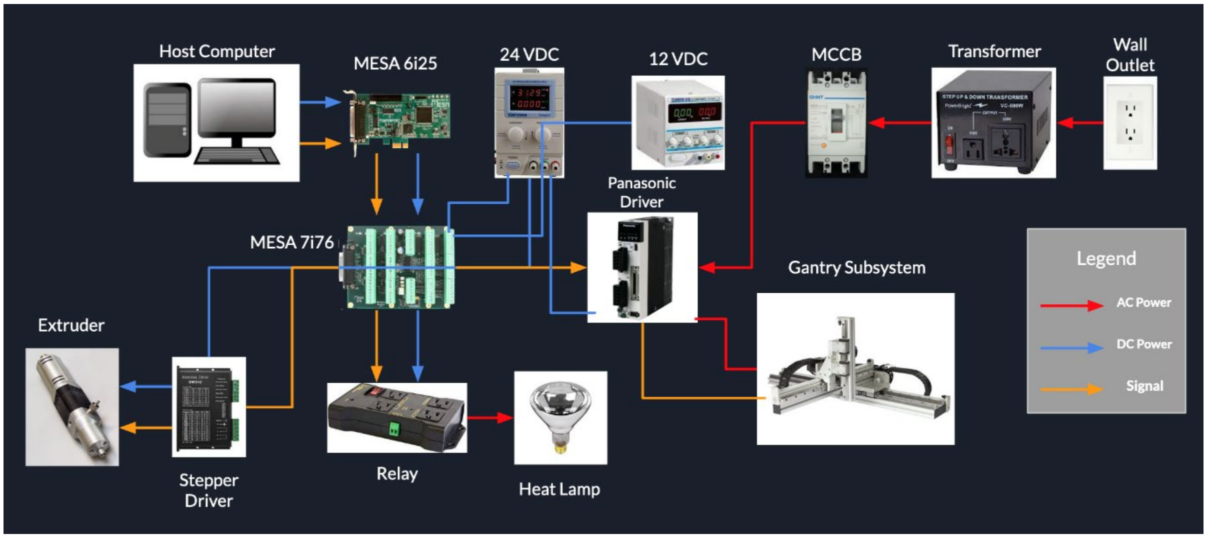

Fig. 5. Electrical system flowchart overview.

A host computer is used to control the entire CODE printer assembly. This computer is installed with the LinuxCNC operating system for suitable compatibility with the remaining electrical components. The host computer was selected such that the desktop latency is minimized; specifically, the computer used has a latency of around 9000 ns. Within LinuxCNC, the PNC configuration wizard is used to setup various system parameters including the programmable boards, PID gains for the motors, inputs, and outputs for the system. The result of the PNC configuration wizard is the generation of. hal and .ini files which includes information that controls the printer assembly when LinuxCNC is run. Furthermore, any later modifications to the printer or the electrical subsystem can be updated by updating these files. The LinuxCNC graphical user interface (GUI) takes an input of G code to control the printer to print the specified part.

The host computer is connected to two different MESA boards, MESA 6i25 and MESA 7i76. The MESA 6i25 is a general purpose programmable I/O card which connects directly to the computer through the computer's peripheral component interconnect express (PCIe) x1 port. The MESA 7i76 is a daughter board that connects directly to the MESA 6i25 board through a DB25 cable. This daughter board is the central component that the communicates with the gantry, extrusion, and heating subsystems.

Two DC power supplies at 24VDC and 12VDC are used within the electrical subsystem to power the MESA boards, servo drivers, limit switches, the electrical relay, and the micro-step driver. Servo drivers are used to control the motors within the linear actuators. These drivers require 220VAC. The US standard wall outlet is connected to a 500W step-up transformer to convert to 220VAC single-phase power. The transformer then connects to a molded case circuit breaker (MCCB), which is then connected to the driver for external power. Moreover, the main communication between the host computer and the servo drivers are through wiring the drivers to the MESA 7i76 board with step and direction pins. The MESA 7i76 board communicates with each driver for x-, y-, and z-axes by sending digital step pulses.

The extruder, which includes a stepper motor, is connected to a micro-step driver, which is then connected to the MESA 7i76 board. Similar to the servo drivers, the micro-step driver is connected to the MESA 7i76 board through step and direction interfaces. The G code read by the host computer is translated through the two separate MESA boards, which then sends signals to both the servo drivers and the micro-step driver to control both the motion and extrusion subsystem, respectively.

The MESA 7i76 board also includes input and output features. The board’s inputs are connected to the limit switches of the motion subsystem to correctly identify the location of each axis as well as to setup a printing envelope and homing sequence. The heat lamp, which requires 120VAC, is connected to an electrical relay that is normally off. This electrical relay is connected to the MESA 7i76 board's output such that the command sent by LinuxCNC either activates or deactivates the heat lamp while printing.

3.2 Pre-processing and Printing Test Specimens

The ceramic slurry is composed of four main components including a ceramic powder, deionized water, a binder, and a dispersant. The ceramic powder used is silicon dioxide powder (SiO2, US Research Nanomaterials, Inc., Houston, TX, USA). The silicon dioxide powder has a purity of 99+%, an average particle size of 400nm, a specific surface area of $48m^2/g$, a bulk density of <0.9 g/cm^3, and a true density between $1.8g/cm^3$ and $2.4g/cm^3$. The crystal phase of the silica powder used is amorphous. Deionized water is used due to its purity with regards to the mineral content. A binder is mainly used to increase the final viscosity of the slurry to be printed as well as to strengthen the printed green body, and a dispersant is primarily used to avoid sedimentation of ceramic particles, which can cause separation and nonhomogeneity within the slurry. The specific binder and dispersant used are cold-water dispersible methylcellulose (CELLOSIZE™ Texture F4M Hydroxypropyl Methylcellulose, Dow Chemical Company, Hayward, CA, USA) and ammonium polymethacrylate (DARVAN® C-N, Vanderbilt Minerals, LLC, Gouverneur, NY, USA). The aforementioned materials are preprocessed using multiple stages displayed visually in a flowchart format in Figure 6 for the final ceramic slurry to be printed.

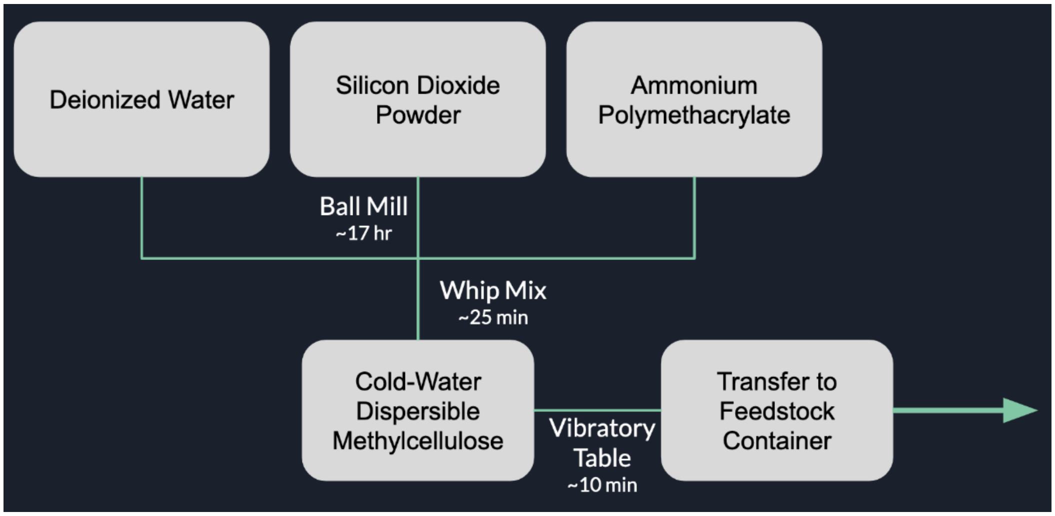

Fig. 6. Visual diagram displaying the multiple stages required for pre-processing the slurry.

The initial ball mill stage includes several parameters, such as ball mill duration, milling container size and material, milling media size and material, and speed at which the ball mill runs. The ball mill duration for the final slurry discussed in this paper is approximately 17 hours derived from Ghazanfari et. al. [9],[10]. The milling container is a cylindrical jar made of high-density polyethylene (HDPE) and has an inner diameter and length of approximately 85mm and 142mm, respectively. The milling media material and size used for the final slurry discussed in this paper are zirconia cylinders with a diameters and length of approximately 9.5mm and 9.5mm, respectively. The critical ball mill speed was calculated based on equation 1, which indirectly depends on the gravitational constant, and directly depends on the inner diameter of the ball mill (R) container and the diameter of one piece of milling media (r) [25]. The final ball mill speed used was between 60% to 65% of the critical ball mill speed, which is approximately 20rpm.

$$Critical\ Speed = \frac{265.45}{\sqrt{(R-r)}} \tag{1}$$

Solids loading is a unitless measurement used to identify the amount of suspended solids in a colloid. Equation 2 displays the solids loading calculation method used for creating the slurry, where V_S is the volume of the solid materials in the slurry and V_T is the total volume. The final ceramic slurry is created to be approximately 55vol% solids loading. This implies that 55% of the total volume of slurry in mL created is composed of solid elements which include silicon dioxide powder and binder.

$$vol\%\ Solids\ Loading = \frac{V_S}{V_T} \tag{2}$$

After research and experimental testing, the initial 60vol% solids loading, derived from Ghazanfari et al., proved to be excessively high, such that modified ball mill speed and duration as well as increasing the milling media amount did not assist in proper mixing. The difference between 60vol% and 55vol% solids loadings can be observed in Figure 7. In the case of 60vol% solids loading, the water is mixed with the ceramic powder such that the top surface is thoroughly mixed; however, when probed, the powder emerges and separates from the slurry. Moreover, the 55vol% solids loading ceramic particles are more homogenously dispersed, and the slurry viscosity is more desirable for the addition of the binder.

Fig. 7. Visual difference between 60 vol% solids loading (left) and 55 vol% solids loading (right) without using binder.

The type of dispersant and the proper amount to be used in the ceramic slurry were determined through literature research as well as experimental testing. Kandi et al., studied the effects of various dispersants and dispersant amounts on the rheological behavior of silica ceramics [26]. The article demonstrates that for the DARVAN C-N dispersant, values between 0wt% and 0.25wt% have the best zeta potential results, which correlates to favorable stability of the slurry and resistance to agglomeration. At a pH value of approximately 8, both 0wt% and 0.25wt% have the largest magnitude of zeta potential value.

Similar to vol% solids loading, the wt% is calculated by the amount of dispersant per the amount of silica powder. The initial findings led to an experimental approach to further narrow the suitable dispersant quantity using sedimentation tests. The tests are conducted with 55vol% solids loading of ceramic slurry including silica powder, deionized water, and DARVAN C-N as the dispersant. The dispersant amounts in the tests start at 0.05wt% of the amount of silica and increases by 0.05wt% of silica until 0.4wt% of silica, while maintaining a constant solids loading. The mixture is ball-milled at every dispersant level and collected as samples in test tubes, shown in Figures 8 and 9. Note that the figures have been slightly edited to increase the contrast to clearly display the separation in the test tubes. Figure 8 displays the test tubes with respective dispersant amounts after four days of settling time, and Figure 9 reveals the samples with respective dispersant amounts after seven days of settling time. The comparison of the two images displays that the samples show separation as expected without significant sedimentation increments over time. Additionally, as expected and suggested by literature, the samples with 0.05wt% of silica to 0.25wt% of silica dispersant amounts performed slightly better in terms of separation than the samples with dispersant amounts of 0.3wt% of silica to 0.4wt% of silica. Nonetheless, out of all the test tube samples, it is visually evident that the 0.05wt% of silica dispersant amount performed the best with the least amount of separation and sedimentation results both after four days and seven days. Furthermore, after 30 days of settling time, the results are consistent with both four- and seven-days settling times, such that the dispersant amount corresponding to 0.05wt% of silica outperformed all other cases. After ball milling the mixture with silica, deionized water, and dispersant, the binder is added.

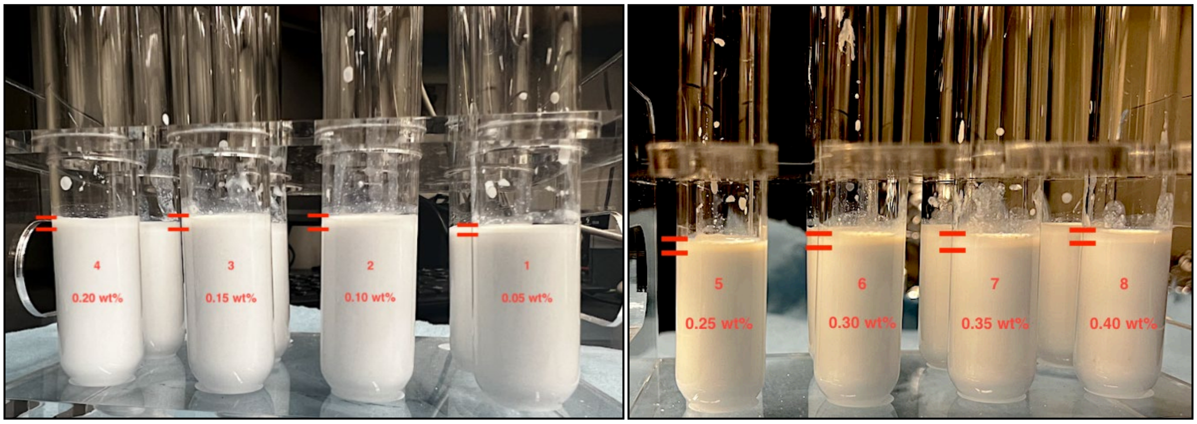

Fig. 8. Sedimentation test results after four days. 0.05wt% of silica to 0.20wt% of silica dispersant amounts (left) from right to left. 0.25wt% of silica to 0.40wt% of silica dispersant amounts (right) from left to right.

Fig. 9. Sedimentation test results after seven days. 0.05wt% of silica to 0.20wt% of silica dispersant amounts (left) from right to left. 0.25wt% of silica to 0.40wt% of silica dispersant amounts (right) from left to right.

Similar to selecting the dispersant, the binder selection was also done through literature research and empirical testing to reach the desired viscosity for extrusion. Initially, cold-water dispersible methylcellulose was chosen to use as binder referenced from [9] and [10]. Silicon dioxide is acidic on the pH scale; however, cold-water dispersible methylcellulose performs better in basic solutions and further polymerizes when combined with silica. Punitha et al. studies that the in a solution of 9.2 pH value, the intermolecular forces are increased [27]. Polyethyleneimine is studied by Gilmer et. al. as a suitable binder when using binder jet additive manufacturing to create strong silica sand structures; however, polymer infiltration was used for post-processing instead of sintering [28]. Moreover, polyvinyl alcohol (PVA) was also tested as a binder for the slurry [29]. PVA performed better with regards to achieving the desired viscosity when premixed with water and added to the slurry; however, the slurry dries much quicker when exposed to air compared to methylcellulose. Due to the present extrusion system which uses compressed air to feed the feedstock to the extruder, the slurry transfer behavior is displayed in Figure 10, which shows that the feedstock dries in various locations within the container which causes clogging and halts the continuous transfer of the slurry to the extruder. Additionally, PVA has a viscosity of approximately 45cP, whereas methylcellulose has a viscosity of approximately 5000cP. The difference in viscosity implies using a much higher amount of PVA to reach the same desired level of slurry viscosity when using methylcellulose. Specifically, for example, 60mL of slurry requires approximately 11.6g of PVA to reach the same viscosity as 0.2g of methylcellulose. This significant increase not only drastically changes the solids loading, but also decreases the strength of the post-processed specimen after performing binder burnout.

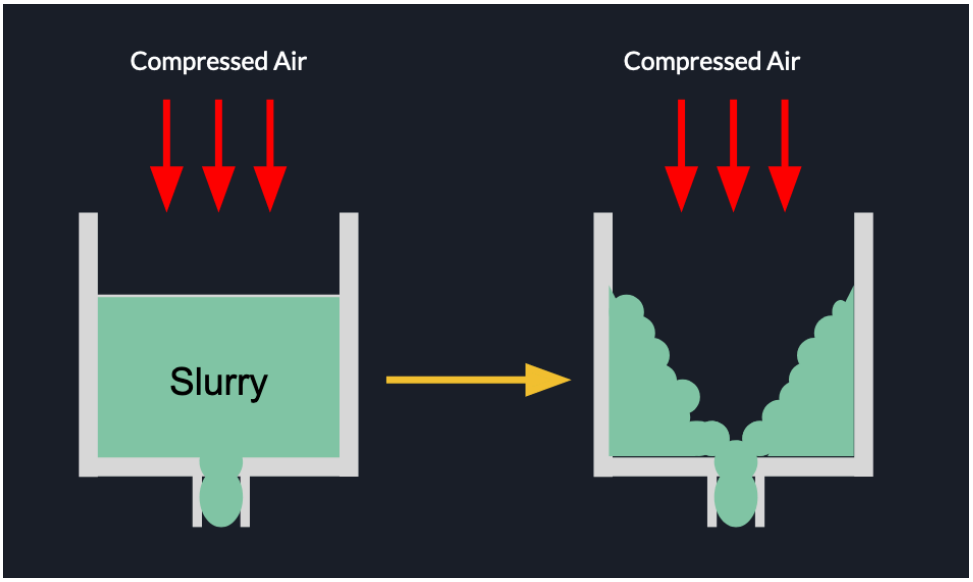

Fig. 10. When PVA is used as binder, the paste near the walls and at the top surface dries when exposed to compressed air such that the feedstock dispenser clogs, and the slurry stops flowing to the extruder.

Therefore, methylcellulose is chosen as the binder for pre-processing the slurry. The polymerization is addressed by following speed and time control when mixing the binder into the slurry. The amount of binder is added in 25% increments and the speed control is displayed in Figure 11. Note that if the slurry does exhibit a non-Newtonian behavior, the speed of mixing is dropped to 20rpm until that phase in the slurry is passed. The binder is mixed into the slurry for around 25 minutes. After mixing the binder, a vibratory table was used for approximately 10 minutes to minimize air bubbles within the slurry, to provide homogenous extrusion while printing.

The amount of material used to create the slurry is calculated for an ASTM standard A-sized bar, which has dimensions of 2mm x 1.5mm x 25mm. However, since post-processing specimens includes shrinkage of each dimension, the printed green body bar size has dimensions of 3mm x 2.25mm x 37.5mm. The approximate shrinkage rate of 15% in all

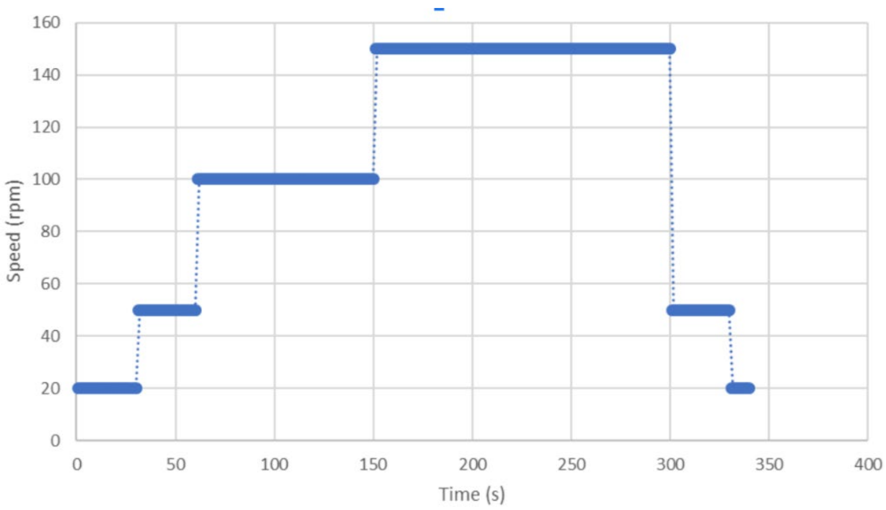

Fig. 11. To overcome the mixing issue with methylcellulose, a speed and time control is used at each addition of binder to the slurry.

dimensions used was derived from [9] and [11]. Therefore, the total volume of one A-sized bar green body is approximately 0.25mL. At 55vol% solids loading, approximately 0.14mL of the slurry is composed of silica and methylcellulose, and the remaining 0.11mL is composed of water and ammonium polymethacrylate. Figure 12 displays an example of values of 60mL of slurry at 55vol% solids loading.

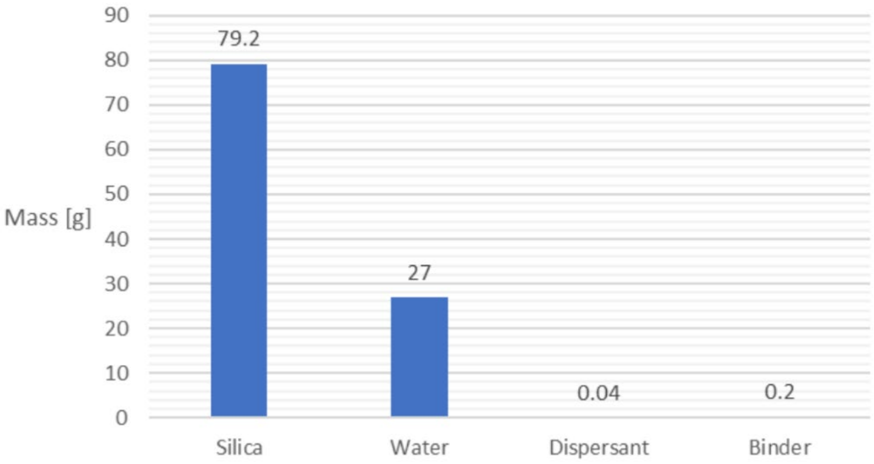

Fig. 12. Visual description of the amounts of each material in a 60mL slurry at 55vol% solids loading.

After pre-processing the slurry, the slurry is transferred into a feedstock container and is printed. SOLIDWORKS is used to model the A-sized bar and is imported to a slicer. Slic3r is used as a slicer, which generates a G code file that is input into LinuxCNC to print. The printing parameters used to print are set in the slicer. The three main printing parameters tuned are the gantry speed, line spacing, and layer thickness as they control the printing in x, y, and z-directions, respectively as shown in Figure 13.

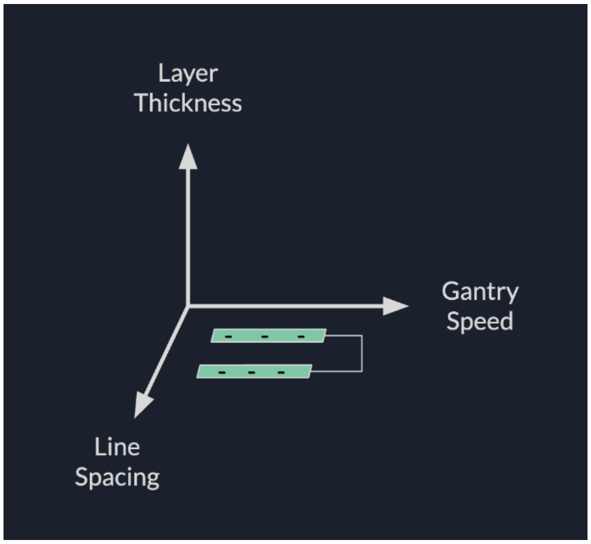

Fig. 13. Three main printing parameters that are finetuned.

After experimental testing and finetuning, Table 2 displays the final parameters used for printing an A-sized bar. The infill pattern chosen results in long straight paths perpendicular to the applied loading in a 3-point bending test. This pattern is selected to achieve higher flexural strength values as studied by Li et. al [30]. An oil bath was not used when printing A-size bar specimens due to the small height of 1.5mm and the low number of layers when printing.

Table 2
Printing Parameters set in the Slicker used to Print A-Sized Bars.

Printing Parameter	Printing Parameter Value
Layer Height	0.5mm
Infill Pattern	Concentric
Combined Gantry Speed	15mm/s
Nozzle Diameter	0.8mm
Line Spacing	0.75mm
Heat Lamp Time	45s
Heat Lamp Distance	0.48m

Figure 14 displays an ASTM A-sized bar being printed with the aforementioned printing parameters. The start-stop condition for extrusion is shown by the lack of stringing, and the viscosity of the deposited layer is shown by the layer not expanding in the lateral directions.

Fig. 14. Example of an ASTM A-sized bar being printed.

3.3 Average Density and Sintering Schedule Tests

After printing the test specimens, post-processing is conducted. There are three main stages to post-processing including drying, binder burnout, and sintering. The drying stage is conducted to remove the water content from the printed green body. This stage is performed in a humidity chamber at two steps. The first step is conducted at 25°C and 75%rH for approximately the first 40 hours and the second step at 40°C and 50%rH for the next 48 hours to ensure complete and safe drying. These values were modified from the reference as studied by Ghazanfari et. al [10]. After drying the test specimens, binder burnout was performed using a sintering furnace at 450°C for 2 hours with a heating rate of 1°C per minute, as thermal degradation of the binder occurs at much lower temperatures than the full densification of the ceramic sample. After debinding, the test specimens are subject to sintering using a sintering furnace. The primary experimental analysis conducted studies the sintering phase of post-processing in CODE, specifically observing the specimen relative bulk density while varying the sintering times and temperatures. All the test specimens used for this experiment have the same geometry while being subject to varied sintering schedules. Five specimens are tested at each sintering schedule. Two main studies were used for reference for obtaining experimental sintering schedules. With epoxy resin as binder for silica ceramics, Zhang et al. used selective laser sintering (SLS) to fabricate specimens [31]. The sintering schedule used in that study had a multi-step process at which different temperature increment rates were used; however, the primary time for full densification was around 6 hours at a heating rate of 3°C/min at a maximum temperature of 1200°C. From this study, 1150°C for 6 hours, 1050°C for 7 hours, and 950°C for 8 hours at the same heating rates are proposed to analyze the behavior of sintering schedules on the part bulk density. Furthermore, Jiang et al. used methylcellulose as binder and printed Si-SiO_2 specimens via DIW [32]. The study indicates that the green bodies were sintered in nitrogen using a two-step sintering process. The study uses a much higher temperature of 1400°C and the total sintering time of 4 hours with a more aggressive heating rate of 5°C/min. Overall, the specific sintering schedules tested are displayed in Table 3. Wangmooklang et. al. informs

Table 3
Sintering Schedules Tested for Observing Resulting Part Density.

No.	Sintering Temperature [°C]	Sintering Time [hr]	Heating Rate [°C/min]
1	950	8	3
2	1050	7	3
3	1150	6	3

that the use of a nitrogen environment while sintering does not significantly affect the part density of silicon nitride ceramics; however, the mechanical properties are increased when sintering in a nitrogen environment [33]. A higher sintering time corresponds to a higher strength value as studied by Pan et. al with 3D printed alumina ceramics [34]. While sintering silica, there are multiple polymorphs that the specimen can transition to depending on the sintering temperature including alpha and beta quartz, alpha and beta tridymite, and alpha and beta cristobalite [35]. These polymorphs are all results of low-pressure sintering. Due to beta tridymite having a strong hexagonal crystal structure, the sintering temperatures chosen to be tested are within the range of the specific silica polymorph, specifically between 870°C and 1470°C. Furthermore, Manière et. al. studies that sintering at a temperature close to 1170°C produces high dense silica specimens [36].

After sintering the test specimens, the bulk density of each of the parts is calculated using equation 3, where ρ is the experimentally calculated bulk density, m is the experimentally obtained specimen mass, and V is the experimentally obtained volume calculated by measuring the sintered part dimensions.

$$\rho = \frac{m}{V} \tag{3}$$

The experimentally obtained bulk density can be divided by the theoretical bulk density of silicon dioxide at the same volume to obtain the relative bulk density. As five specimens are tested at each sintering schedule, the average is obtained to report the average bulk density for each sintering schedule.

3.4 Flexural Strength Tests

To study the research hypothesis, the central experiment is performing mechanical tests on ceramic silicon dioxide test specimens created using CODE to study the flexural strength of each test specimen. The 3-point bending test via an Instron universal testing machine is used following the ASTM C1161 standard [37]. This test is performed for four specimens of the same ASTM A-sized bar geometry at each sintering schedule with a 3-point bending fixture, as displayed in Figure 15. Additionally, after obtaining the results, the mean flexural strength value is reported.

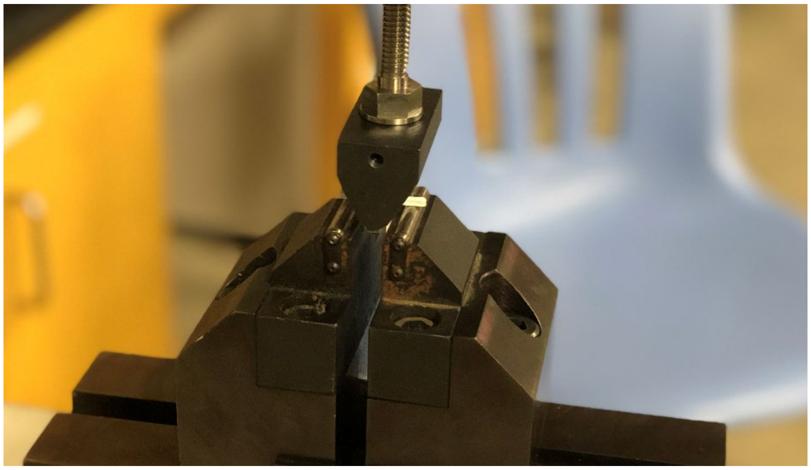

Fig. 15. 3-point bending test fixture setup on the Instron universal testing machine.

4 RESULTS AND DISCUSSION

4.1 Effects of Sintering Schedules on Density

Printed ceramic green bodies are subject to post-processing including drying, debinding, and sintering. The sintering schedules studied are performed after consistent drying and debinding for all parts. Table 4 displays the sintering schedule and average density for the corresponding sintering schedule.

Table 4
Sintering Schedules and Average Density.

Sintering Temperature [°C]	Sintering Time [hr]	Average Part Density [g/cm^3]
950	8	1.24
1050	7	1.23
1150	6	1.15

From the obtained results, the variation of the sintering schedules did not significantly influence the sintered part density. Higher sintering temperatures and higher solids loading of the slurry can be studied to increase the overall part density. Furthermore, increased sintering times at the respective sintering temperatures could aid in increasing the density values. The densities achieved are approximately 50% of the theoretical density of silica. The low-density values in relation to the theoretical density of silica could be attributed to porosity within the sintered specimen from the air pockets introduced when pre-processing the slurry. The air pockets could be attributed to the mixing of the slurry when adding the binder as well as the method of transferring the slurry from the mixing container into the feedstock holding container for extrusion. With regards to the mixing, lower speeds could be used for less agitation resulting in less air mixed into the slurry, but this would lead to significantly longer pre-processing times. A two-stage mixing process could also be used such that the slurry is initially mixed at low speeds, and high-speed mixing time could be reduced. Due to porosity being the main defect for lower part densities, the minimizing of air pockets would substantially improve the overall density values.

4.2 Flexural Strength of Parts at Varied Sintering Schedules

The flexural strengths of CODE printed ceramics components are measured after post-processing. The flexural strength values are calculated using equation 4 obtained from the ASTM C1161 standard, which depends on the break force (P), the testing support span (L), the specimen width (b), and the specimen height (d).

$$S = \frac{3PL}{2bd^2} \tag{4}$$

Four test specimens at each sintering schedule are tested and the average flexural strengths are displayed in Table 5. Comparing Tables 4 and 5, a trend can be observed that the lower the density values, the higher the flexural strength values.

Table 5
Sintering Schedules and Average Flexural Strength.

Sintering Temperature [°C]	**Sintering Time [hr]**	**Average Flexural Strength [MPa]**
950	8	3.01
1050	7	3.2
1150	6	3.52

An example of a load vs. time curve and a stress vs. strain curve for a test specimen sintered at 1150°C for 6 hours is obtained from the Instron machine and is shown in Figure 16. These graphs exhibit a behavior typical to a ceramic material. The low strain and the immediate drop in stress and load after fracture of the test specimen can be seen. The values obtained from the flexural strength tests are much lower than values obtained from literature

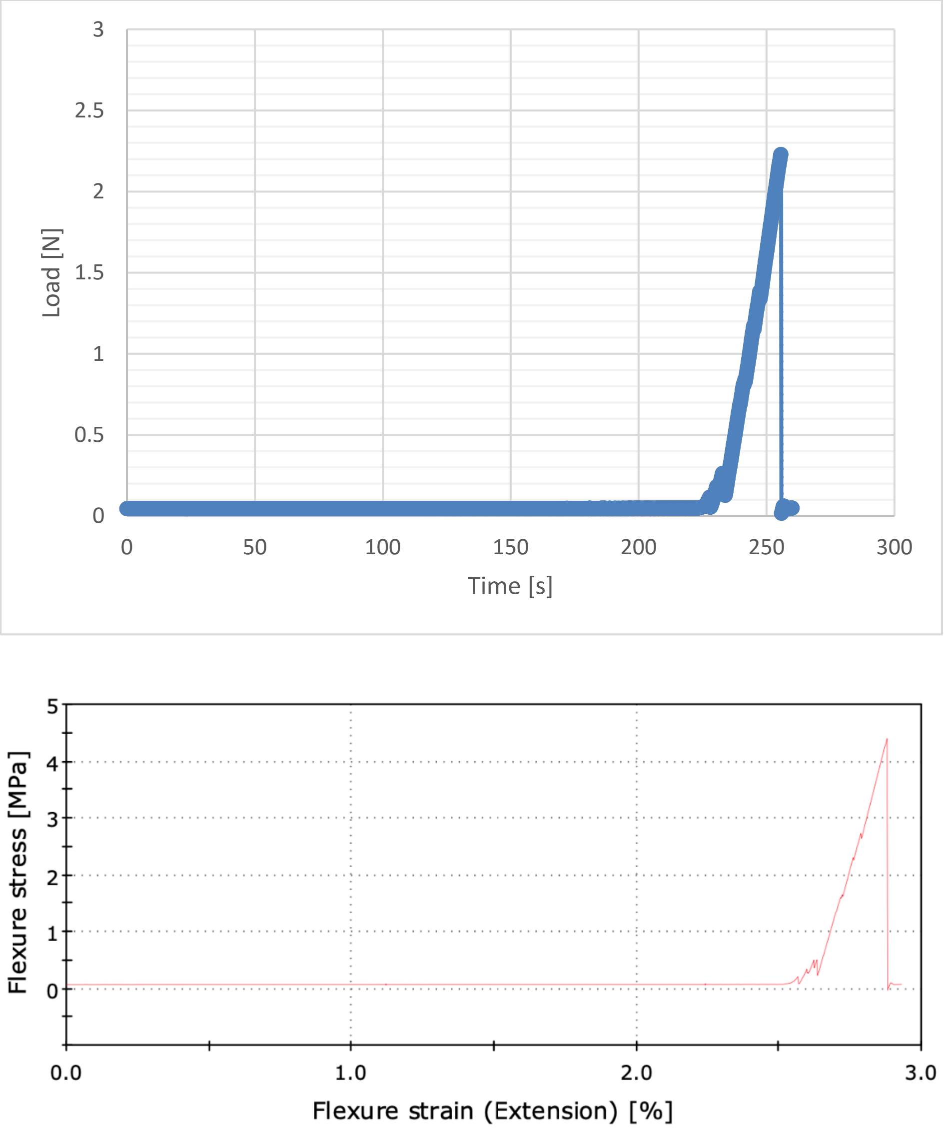

Fig. 16. Load vs. time (top) and stress vs. strain (bottom) curves display a constant application and immediate drop of the load and stress after the fracture of the test specimen.

of other additive manufacturing methods. Similar to the density values, the main reason for this discrepancy is due to porosity within the printed and sintered specimens. The porosity is influenced by air bubbles while pre-processing the feedstock. Specifically, performing the multi-stage addition and mixing of the binder to avoid polymerization of the binder is also theorized to introduce air at each addition. This leads to air pockets and uneven extrusion while printing, causing the porosity to propagate to the post-processing and testing stages. Additionally, the pores left by water evaporation while drying and binder while debinding could influence the final part porosity as well. Due to the slurry being created at 55vol% solids loading, approximately 45vol% of the printed part contains water, which when evaporated can leave pores in its place. An even higher sintering temperature could assist in the full densification of the printed part.

After performing the flexural strength 3-point bending tests, a sample was studied under a microscope to observe the fracture point as well as the specimen cross-section, displayed in Figure 17. The defects including air bubbles when printed can be observed due to pre-processing of the slurry. Due to this, the sintered part is drastically weakened, resulting in low flexural strength values.

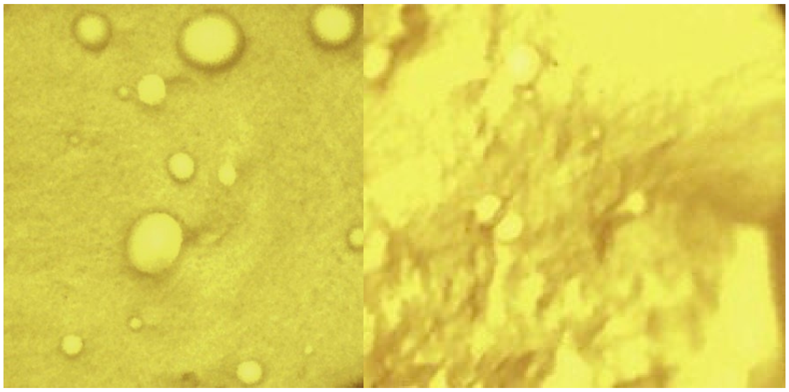

Fig. 17. Cross-sectional images of tested sample, displaying defects within the part.

The created air bubble pockets could be attributed to the aforementioned issue with whip mixing the slurry with air inside the container and inconsistent transfer of the slurry to the feedstock holder, such that new air bubbles are introduced. Additionally, due to the tubing connecting the feedstock holding container to the extruder being relatively long, the flow of the slurry within the tube can be hindered due to the air bubbles. Furthermore, an increased time for pre-processing the slurry on the vibratory table is theorized to reduce the air pockets within the viscous slurry.

Lowering porosity due to air bubbles and increasing solids loading could lead to higher strength values. Additionally, using a crystalline silica powder as opposed to an amorphous structure while adding sintering aids, would increase the part strength. However, the post-processing stage did not result in any cracks or warpages due to high drying and heating rates. Post-processing including surface griding, which increases the surface quality of the test specimen, could increase the flexural strength values as well. Addressing the mixing of the paste, a two-stage or separate vacuuming after mixing could be used to reduce the air pockets within the paste. Additionally, a shorter tubing for the transfer of the feedstock to the extruder would assist in better flow of the material as well. An improved method for transferring the feedstock from the mixing container into the final syringe would aid in reduction of gaps in the slurry due to air pockets. Overall, comparing Tables 1 and 5, the flexural strengths of silica parts printed by CODE have lower values due to pre-processing defects; however, adjusting and modifying the pre-processing stage such that air pockets are drastically reduced and minimized could lead to similar strength values as displayed in Table 1.

5 FUTURE WORK

Future work entails three different avenues in which testing silica with CODE could be performed including pre-processing, post-processing, and testing. Within pre-processing, the silica colloid could be tested with varying binders. Rather than solely using either methylcellulose or PVA, a combination of the two could be tested. Another method would be to modify the pH level of the silica solution by adding a basic hydroxide compound such that the polymerization of methylcellulose could be completely avoided. This process would not only increase the paste viscosity for better printing quality, but also assist in improving the printed green body strength. Increasing solids loading could also be performed by modifying the milling media and the milling container sizes while ball-milling the slurry. As previously mentioned, instead of using amorphous silica, a crystalline silica crystal structure powder could be used to improve part strength, while adding sintering aids such as FeO and CaO to minimize the effects of drastic volumetric changes during silica polymorphic transitions while sintering. Moreover, air bubble reduction in the slurry by using a two-step mixing process, in which the mixing is performed first, and the slurry is then subject to a vacuum to remove the air pockets could assist in a more homogenous extrusion of the feedstock while printing, resulting in higher part flexural strengths. Furthermore, an improved mechanism of paste transfer to the feedstock holding container would improve the air bubble concern as well. Future work with regard to printing composites using silica can be conducted as well to study the efficacy of the CODE printer on composites as well as printing complex geometries with an oil bath to better preserve the structure and strength of the green body due to uneven evaporation.

Additional work with regards to the post-processing stage could be performed including surface grinding the sintered specimen, modifying the sintering schedule with a multi-stage process, and performing pressurized sintering. Surface grinding the sintered specimen can provide a more uniform surface and reduce surface imperfections such as pores and uneven smoothness. This process can assist with increasing the flexural strength of the test specimen by avoiding the surface defects’ influence in crack propagation while performing a 3-point bending test. Additionally, modifying the sintering stage of post-processing with testing multi-stage as well as pressurized sintering could be performed to increase the densification of the test specimen.

Further work with testing the sintered test specimens for other mechanical properties such as fracture toughness, hardness, compressive strength, and tensile strength could be performed to fully analyze the silica part printed by CODE. Moreover, a fractographic analysis could be performed to further study the fracture of the test specimen when subject to a 3-point bending test. A fractographic analysis can provide a detailed analysis of the fracture of the test specimen, specifically with regards to the cause of the fracture. This process can assist in identifying the influence of defects such as large grain sizes or air pockets on the final flexural strength values of the tested part.

6 CONCLUSION

In conclusion, a 55vol% solids loading slurry is created using silicon dioxide powder, deionized water, cold-water dispersible methylcellulose, and ammonium polymethacrylate at corresponding material ratios. The printed and sintered ASTM A-sized bars are subject to a 3-point bending test according to the ASTM C1161 standard. Both the density and flexural strength values are lower with printing using CODE when compared to other current additive and conventional manufacturing methods as described in section 2. The main reason for this can be attributed due to defects within the printed parts including porosity due to air pockets and insufficient viscosity when pre-processing the slurry. Future work and approaches to minimize these defects could be performed to print high-strength silicon dioxide parts using CODE. Such approaches include adjusting the pH level to avoid polymerization of cold-water dispersible methylcellulose to increase the viscosity of the printed part as well as improve the green-body strength due to addition of a higher quantity of binder. A two-step mixing process could be used to mix the binder to further reduce the air bubbles within the feedstock to provide consistent extrusion while printing. Additional methods as outline in the previous section can also be used to aid in reduction of the part defects.

REFERENCES CITED

[1] Z. Chen *et al.*, “3D printing of ceramics: A review,” *J. Eur. Ceram. Soc.*, vol. 39, no. 4, pp. 661–687, Apr. 2019.

[2] Beamler. “3D Printing with Technical Ceramics.” https://www.beamler.com/3d-printing-with-technical-ceramics/ (accessed Nov. 6, 2022).

[3] N. C. Lawson and J. O. Burgess. “Dental Ceramics: A Current Review.” Europe PMC. https://europepmc.org/article/med/24773195 (accessed Nov. 6, 2022).

[4] UCSB Science Line. “Why Only Silicon Chip is Used in Computers? Does it Have Any Special Property?” http://scienceline.ucsb.edu/getkey.php?key=4527 (accessed Nov. 6, 2022).

[5] Heraeus Group. “Fused Silica for Semiconductor Manufacturing.” https://www.heraeus.com/en/hca/industries_and_applications_hca/semiconductor_industry_hca/semiconductor_industry_hca.html (accessed Nov. 8, 2022).

[6] Wikipedia. “Silicon Dioxide.” https://en.wikipedia.org/wiki/Silicon_dioxide (accessed Nov 8, 2022).

[7] Inderscience Publishers. “Using Silicon Dioxide as a Binding Layer for Replacement Bone Prosthetics.” Phys.org. https://phys.org/news/2014-06-silicon-dioxide-layer-bone-prosthetics.html (accessed Nov. 8, 2022).

[8] F. Romero-Gavilan *et al.*, “Bioactive potential of silica coatings and its effect on the adhesion of proteins to titanium implants,” *Colloids Surf., B*, vol. 162, pp. 316–325, Feb. 2018.

[9] A. Ghazanfari *et al.*, “Mechanical characterization of parts produced by ceramic on-demand extrusion process,” *Int. J. Appl. Ceram. Technol.*, vol. 14, no. 3, pp. 486–494, Jan. 2017.

[10] A. Ghazanfari *et al.*, “A novel freeform extrusion fabrication process for producing solid ceramic components with uniform layered radiation drying,” *Addit. Manuf.*, vol. 15, pp. 102–112, May 2017.

[11] A. Ghazanfari *et al.*, “Additive manufacturing and mechanical characterization of high density fully stabilized zirconia,” *Ceram. Int.*, vol. 43, pp. 6082–6088, Feb. 2017.

[12] W. Li *et al.*, “Characterization of zirconia specimens fabricated by ceramic on-demand extrusion,” *Ceram. Int.*, vol. 44, no. 11, pp. 12245–12252, Aug. 2018.

[13] T. Yu *et al.*, “Extrusion-based additive manufacturing of yttria-partially-stabilized zirconia ceramics,” *Ceram. Int.*, vol. 46, no. 4, pp. 5020–5027, Mar. 2020.

[14] *Standard Test Method for Vickers Indentation Hardness of Advanced Ceramics*, ASTM C1327-15, ASTM International, West Conshohocken, PA, USA, 2015.

[15] Y. Lu *et al.*, “Flexural strength and weibull analysis of Y-TZP fabricated by stereolithographic additive manufacturing and subtractive manufacturing,” *J. Eur. Ceram. Soc.*, vol. 40, no. 3, pp. 826–834, Mar. 2020.

[16] B. J. Briscoe and N. Özkan, “Characterization of ceramic pastes by an indentation hardness test,” *J. Eur. Ceram. Soc.*, vol. 17, no. 14, pp. 1675–1683, 1997.

[17] W. Li *et al.*, “Extrusion-based additive manufacturing of functionally graded ceramics,” *J. Eur. Ceram. Soc.*, vol. 41, no. 3, pp. 2049–2057, Mar. 2021.

[18] W. Li *et al.*, “Fabricating ceramic components with water dissolvable support structures by the ceramic on-demand extrusion process,” *CIRP Ann.*, vol. 66, no. 1, pp. 225–228, 2017.

[19] Y. Y. Wang *et al.*, “Fabrication of dense silica ceramics through a stereo lithography-based additive manufacturing,” *Solid State Phenom.*, vol. 281, pp. 456–462, 2018.

[20] I. Cooperstein *et al.*, “Additive manufacturing of transparent silica glass from solutions,” *ACS Appl. Mater. Interfaces*, vol. 10, no. 22, pp. 18879–18885, May 2018.

[21] X. Wang *et al.*, “Microstructure and properties evolution of silicon-based ceramic cores fabricated by 3D printing with Stair-stepping effect control,” *J. Eur. Ceram. Soc.*, vol. 41, no. 8, pp. 4650–4657, Jul. 2021.

[22] S. Yin *et al.*, “Porous fused silica ceramics prepared by gelcasting using multigrade fused silica powders,” *J. Alloys Compd.*, vol. 819, p. 152982, Apr. 2020.

[23] C. Xu *et al.*, “Cellular silica-based ceramics prepared by direct foaming at high temperature,” *Ceram. Int.*, vol. 36, no. 3, pp. 923–927, Apr. 2010.

[24] Y. Wang *et al.*, “Additive manufacturing of silica ceramics from aqueous acrylamide based suspension,” *Ceram. Int.*, vol. 45, no. 17, pp. 21328–21332, Dec. 2019.

[25] P. O. Abbe. “Variables in Ball Mill Operation.” https://www.pauloabbe.com/variables-in-ball-mill-operation (accessed Nov. 4, 2022).

[26] K. K. Kandi, S. K. Pal, and C. S. Rao, “Effect of dispersant on the rheological properties of gelcast fused silica ceramics,” *IOP Conf. Ser.: Mater. Sci. Eng.*, vol. 149, p. 012063, Jul. 2016.

[27] S. Punitha, R. Uvarani, and A. Panneerselvam, “Effect of pH in aqueous (hydroxy propyl methyl cellulose) polymer solution,” *Results Mater.*, vol. 7, p. 100120, Sep. 2020.

[28] D. B. Gilmer *et al.*, “Additive manufacturing of strong silica sand structures enabled by polyethyleneimine binder,” *Nat. Commun.*, vol. 12, no. 5144, Aug. 2021.

[29] G. P. Goldschmidt *et al.*, “Production and characterization of 3D-printed silica-based cellular structures,” *Open Ceram.*, vol. 9, p. 100225, Mar. 2022.

[30] H. Li *et al.*, “Improved mechanical properties of silica ceramic cores prepared by 3D printing and Sintering Processes,” *Scr. Mater.*, vol. 194, p. 113665, Mar. 2021.

[31] J. Zhang *et al.*, “Effects of particle grading on properties of silica ceramics prepared by Selective Laser Sintering,” *Ceram. Int.*, vol. 48, no. 1, pp. 1173–1180, Jan. 2022.

[32] Q. Jiang *et al.*, “Fabrication and properties of si2n2o-si3n4 ceramics via direct ink writing and low-temperature sintering,” *Ceram. Int.*, vol. 48, no. 1, pp. 32–41, Jan. 2022.

[33] N. Wangmooklang *et al.*, “Properties of Si3N4 ceramics sintered in air and nitrogen atmosphere furnaces,” *J. Ceram. Soc. Jpn.*, vol. 115, no. 1348, pp. 974–977, Dec. 2007.

[34] Y. Pan *et al.*, “Effect of holding time during sintering on microstructure and properties of 3D printed alumina ceramics,” *Front. Mater.*, vol. 7, Apr. 2020.

[35] The Quartz Page. “The Silica Group.” http://www.quartzpage.de/gen_mod.html (accessed Nov. 5, 2022).

[36] C. Manière *et al.*, “Modeling sintering anisotropy in ceramic stereolithography of silica,” *Acta Mater.*, vol. 182, pp. 163–171, Jan. 2020.

[37] *Standard Test Method for Flexural Strength of Advanced Ceramics at Ambient Temperatures*, ASTM C1161-13, ASTM International, West Conshohocken, PA, USA, 2013.